# Optical, Magnetic and Electrochemical Properties of Spinel $Mn_3O_4$, $Co_3O_4$ Nanostructures

Dr. Dadamiah PMD Shaik[1], Associate Professor,
Dept. of Physics, Vardhaman College of Engineering,
Hyderabad, Telangana-501218

Dr. Md Sameer Ahmed[2,] Associate Professor,
Dept. of Chemistry, Lords Institute of Engg & Tech.
Hyderabad, Telangana-500091

**ABSTRACT**

Manganese oxide ($Mn_3O_4$) and Cobalt oxide ($Co_3O_4$) nanocrystals were synthesized using a straightforward and cost-effective combustion method. Structural analysis through XRD, Raman Spectroscopy, and Fourier Transform Infrared Spectroscopy confirmed the tetragonal structure with I41/amd (141) space group for $Mn_3O_4$ and the cubic structure with Fd3m (227) space group for $Co_3O_4$. The average crystallite sizes were determined using the Debye Scherer formula, resulting in approximately 14 nm for $Mn_3O_4$ and 22 nm for $Co_3O_4$. SEM images displayed irregular and uniform spherical grains for $Mn_3O_4$ and $Co_3O_4$, respectively, with average grain sizes of 100 nm and 120 nm. EDS and XPS spectra showed clear binding energy peaks for Manganese, Cobalt, and Oxygen, confirming the chemical purity of the samples. The optical band gap of the nanocrystals was found to be 2.93 eV for $Mn_3O_4$ and 2.50 eV for $Co_3O_4$. Magnetic analysis revealed a strong ferromagnetic nature at 5 K temperature for both $Mn_3O_4$ and $Co_3O_4$ nanocrystals. Electrochemical investigations demonstrated that $Mn_3O_4$ nanocrystals exhibited excellent performance as electrodes for electrochemical capacitors. At a current density of 0.5 A $g^{-1}$, they achieved a high specific capacitance of 417 F $g^{-1}$, maintaining almost 100% coloumbic efficiency after 600 cycles and displaying good cyclic stability for up to 10,000 cycles. On the other hand, $Co_3O_4$ showed inferior electrochemical behavior, indicating that $Mn_3O_4$ nanocrystals possess superior mass transport of electrolyte ions into the electrode, making them more suitable for electrochemical capacitors.

**Keywords**—Spinel $Mn_3O_4$ and $Co_3O_4$ nanocrystals, band gap, specific capacitance, cyclability.

## I. INTRODUCTION

Lately, electrochemical capacitors have risen to prominence as potential energy storage solutions, thanks to their favorable attributes including extended cycle longevity and impressive energy and power densities [1]. Prior investigations highlight that the efficacy of supercapacitors is notably shaped by the selection of electrode substance and electrolyte. Transition metal oxides and conductive polymers are frequently harnessed as dynamic electrode materials, yielding substantial capacitance but encountering challenges in sustained cycling efficiency due to faradaic redox reactions [2, 3]. Alternatively, carboneous electrodes offer better cyclability but lower capacitance, relying on double-layer capacitance between the electrode and electrolyte.

Among transition metal oxides, some like $Ru_2O$, $MoO_3$, $V_2O_5$, $Fe_2O_3$, $Mn_3O_4$, CuO, ZnO, $MnO_2$, $Co_3O_4$, NiO, and $TiO_2$ have received extensive attention for their high theoretical specific capacitance [4, 5].

Among these, $RuO_2$ is well-studied for its high conductivity, specific capacitance, and chemical stability. However, its limited abundance and high cost hinder practical applications. Spinels like $Mn_3O_4$ and $Co_3O_4$ are considered attractive electrode materials due to their cost-effectiveness, eco-friendliness, and intrinsic high capacity [6-11]. These materials have diversified utility across an array of domains, encompassing rechargeable lithium-ion batteries, molecular adsorption, electrochemistry, magnetism, and supercapacitors. Furthermore, their remarkable catalytic aptitude in oxygen reduction and reaction (ORR) renders them indispensable for ORR catalysis. Beyond that, the distinct magnetic attributes exhibited by these nanoparticles have kindled interest for their conceivable roles in data storage, magnetic particle imaging, wastewater treatment, and other prospective applications [13, 14].

Spinel ferrites and their composites have also found applications in diverse areas, thanks to their unusual magnetodielectric properties. For example, substituted spinel ferrites synthesized through various methods have been utilized in anti-cancer and functional radio electronic devices, catalysis, and biological applications [15-20].

However, there is limited research comparing the magnetic and electrochemical properties of spinel $Mn_3O_4$ and $Co_3O_4$ nanocrystals prepared via combustion synthesis. While various methods exist for synthesizing oxide nanoparticles, combustion synthesis stands out due to its simplicity, low temperature, and short processing time. This article aims to investigate and compare the optical, magnetic, ac capacitance, and electrochemical properties of spinel $Mn_3O_4$ and $Co_3O_4$ nanocrystals. The study reveals that $Mn_3O_4$ nanocrystals outperform $Co_3O_4$, attributed to their high spin and suitable structure with a smaller crystallite size [23, 24].

## II. EXPERIMENTAL PROCEDURE

The reagents utilized in synthesizing spinel $Mn_3O_4$ nanocrystals were provided by the Merck Company and possessed a purity level of over 99%. The preparation involved using manganese nitrate as the oxidant and urea as the fuel, mixed in a 1:1 molar ratio. The oxidant and fuel mixture was dissolved in 30 ml of deionized water and stirred for approximately 30 minutes using a magnetic stirrer. The resulting solution was collected in a quartz crucible and then placed inside a preheated muffle furnace set at 300 ºC for a duration of 30 minutes. After the chemical reaction was complete, the final product was allowed to cool naturally to room temperature and carefully collected. The detailed step-by-step procedure for the solution combustion technique used to prepare $Mn_3O_4$ nanocrystals is depicted in the accompanying flowchart. The same experimental procedure was replicated for the synthesis of $Co_3O_4$ nanocrystals.

.

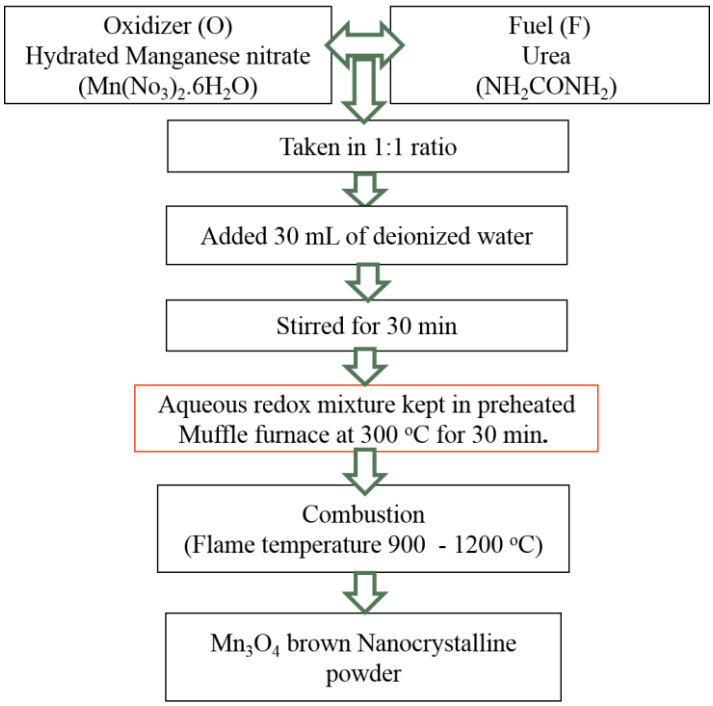


**Schematic diagram of solution combustion technique**

**A. Materials Characterizations**

The structural attributes of the synthesized $Mn_3O_4$ and Co3O4 nanocrystals were investigated employing both X-ray powder diffractometer (XRD-Model 3003 TT) and Raman spectrometer (Horiba Jobin Yvon Lab RAM HR800UV). To deduce the vibrational modes, Fourier Transform Infrared spectrometer (FTIR-ALPHA interferometer, Bruker) was employed. Morphological evaluation along with elemental analysis was executed utilizing Scanning Electron Microscopy (SEM) and Energy Dispersive Spectroscopy (EDS) (Carl ZEISS Model EVO MA15).

For the analysis of chemical states, X-ray Photoelectron Spectrometer (XPS) was employed. Both survey and core-level high-resolution spectra were acquired employing a monochromatic Al Kα X-ray (1486.6 eV) under a vacuum level of 10−9 Torr. The experiment employed an applied beam current of 9 mA and an acceleration voltage of 13 keV (117 W). To investigate the optical band gap, a UV-Vis spectrometer was utilized.

For studying the magnetic properties, Vibrational Sample Magnetometer (VSM) was employed. The electrochemical characteristics of the nanocrystals were evaluated through Cyclic Voltammetry (CV), Chronopotentiometry (CP), and Electrochemical Impedance Spectroscopy (EIS) investigations, which were performed using a 608CHI electrochemical analyzer.

**B. Preparation of Electrodes**

To construct the electrode, a blend comprising the synthesized $Mn_3O_4$, carbon black, and PVdF in an 80:10:10 proportion is subjected to grinding for thirty minutes. The resultant mixture is then integrated with N-

methyl-2-pyrrolidone solvent to yield a slurry. This slurry is applied onto a chemically treated Nickel foam substrate using a brush. The coated electrode is subsequently air-dried at 100°C for a duration of two hours.

To assess the electrochemical performance of the synthesized $Mn_3O_4$ nanocrystals, a glass cell is constructed. This cell comprises a working electrode embedded with the prepared $Mn_3O_4$, with a platinum foil serving as the reference electrode, and Ag/AgCl functioning as the counter electrode. The cell is then filled with a 1M $Na_2SO_4$ aqueous solution. Subsequently, a parallel procedure is executed to prepare the $Co_3O_4$ nanocrystal electrode, enabling subsequent investigation.

## III. RESULTS AND DISCUSSION

### A. Microstructural Properties

The structural analysis of the synthesized $Mn_3O_4$ and $Co_3O_4$ nanocrystals was conducted through X-ray powder diffraction (XRD) across a Bragg's angle range of 10°-70°. Figure 1a displays the XRD pattern of $Mn_3O_4$, revealing diffraction peaks at 19.43°, 33.48°, 38.18°, 44.33°, 49.83°, 59.06°, 60.68°, and 64.96°, corresponding to (101), (103), (004), (220), (105), (321), (224), and (440) reflections, respectively. Additionally, a predominant (211) orientation peak was observed at $2\theta = 36.3°$. These distinct peaks substantiate the tetragonal structure of $Mn_3O_4$, affiliated with the 141/amd (141) space group as identified by JCPDS card No. 89-4837. The lattice parameters are derived as a = b = 5.763 Å and c = 9.456 Å [15]. The pronounced intensity and broadening of these peaks indicate a notable crystallinity level paired with a relatively smaller crystallite size.

Figure 1b illustrates the XRD pattern of $Co_3O_4$, which shows a major (311) orientation peak at $2\theta = 37.19°$, along with other characteristic peaks at 31.54°, 38.68°, 44.59°, 55.31°, 59.55°, and 65.35° corresponding to (220), (222), (400), (422), (333), and (440) reflections. All discernible peaks are aligned with the cubic structure displaying an Fd3m (227) space group, characteristic of a conventional spinel structure. The calculated lattice constant stands at a = b = c = 8.072 Å [15].

The determination of the crystallite size (D) for the samples employed Debye-Scherer's formula (1), resulting in sizes of 14 nm for $Mn_3O_4$ and 22 nm for $Co_3O_4$, correspondingly.

$$D = \frac{k\lambda}{\beta \cos\theta} \qquad \text{----} \qquad (1)$$

where k=0.94, λ=1.5406 Å, β=Width of the diffraction peak at half intensity in radian and θ=Bragg's angle in degrees.

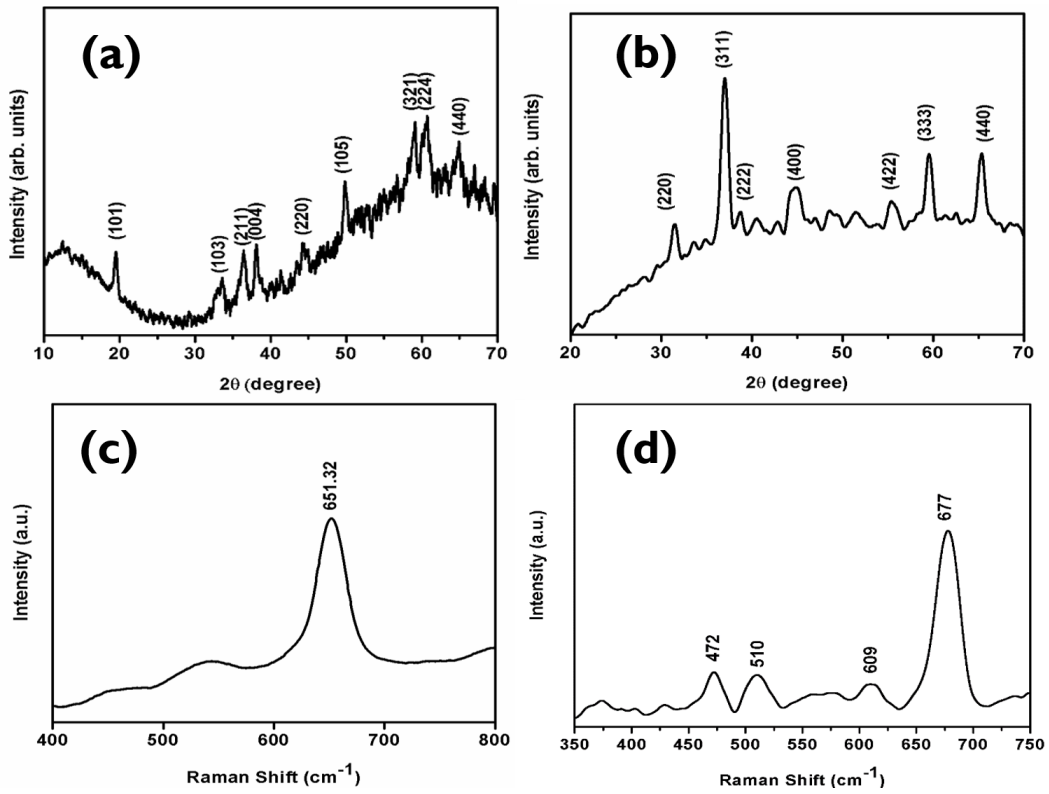


**Figure 1: XRD spectra and Raman spectra of spinel (a, c) $Mn_3O_4$, (b, d) $Co_3O_4$**

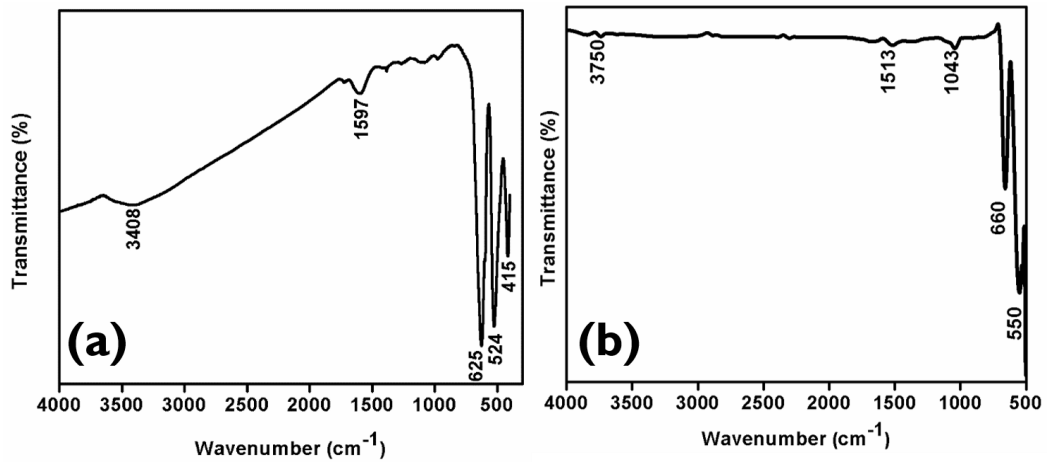


**Figure 2 (a): FTIR spectrum of spinel $Mn_3O_4$ and (b) $Co_3O_4$**

To validate the structure of the synthesized $Mn_3O_4$ and $Co_3O_4$ nanocrystals, Raman spectroscopy was implemented. In Figure 1c, the Raman spectrum of $Mn_3O_4$ unfolds within the wavenumber span of 400-800 cm-1. The discernible peak at 651.32 cm-1 corresponds to the singularly degenerate A1g symmetry mode, attributing to the Mn-O stretching vibrations of $Mn^{2+}$ in tetrahedral coordination [25]. A marginal blue shift of this peak signifies a reduced crystallite size, thereby corroborating the findings from XRD [26]. As portrayed in Figure 1(d), the Raman spectrum of $Co_3O_4$ nanocrystals spans the Raman shift domain of 350-750 cm-1. The robust band near 670 cm-1, along with a cluster of less intense bands spanning 400-600 cm-1, constitutes hallmark features of Co3O4. The potency of the peak at 677 cm-1 and the presence of two feeble peaks at 609 and 510 cm-1 align with A1g, F2g (1), and F2g (2) vibrations, correspondingly. These vibrations correspond to

Co-O stretching, Co-O-Co asymmetric stretching, and Co-O bending modes. Additionally, a faint resonance at 472 cm-1 signifies Eg, a doubly degenerate symmetry mode. These distinctive peaks validate the cubic structure inherent in $Co_3O_4$ [27].

FTIR spectra were acquired for the $Mn_3O_4$ and $Co_3O_4$ nanocrystals, encompassing wavenumbers ranging from 4000 to 500 cm-1, to assess the existence of vibrational bonds within the samples (Fig. 2a&b). As illustrated in Figure 2a, absorption peaks emerge at 625 and 524 cm-1, correspondingly aligning with the Mn-O stretching mode of tetrahedral and octahedral sites. Furthermore, a feeble absorption peak at 415 cm-1 is linked to the vibration of manganese within an octahedral site. Notably, vibrational bands at 1513 and 3750 cm-1 correspond to O-H bending vibrations [25]. Turning to Figure 2b, absorption peaks at 550 and 660 cm-1 correlate with vibrations of $Co^{3+}$ and $Co^{2+}$ in octahedral and tetrahedral sites, respectively. These FTIR analyses affirm the presence of Mn-O and Co-O bonds, thereby reinforcing the outcomes derived from Raman spectroscopy.

The morphology of the $Mn_3O_4$ and $Co_3O_4$ nanocrystals underwent scrutiny via Scanning Electron Microscopy (SEM), with the findings depicted in Figure 3. SEM images reveal the $Mn_3O_4$ sample's composition as irregularly shaped grains with uneven distribution, featuring a typical size of 100 nm (Fig. 3a&b). In contrast, $Co_3O_4$ nanocrystals exhibit homogenous distribution, adopting a spherical grain form, with an average sphere size of 120 nm (Figure 3c&d).

For elemental analysis, Energy Dispersive Spectroscopy (EDS) was employed. As depicted in Figure 3e, the binding energy peaks of Manganese and Oxygen present atomic percentages of 40.91 and 59.09, respectively. This equates to a metal-to-oxygen ratio of 0.69 for the $Mn_3O_4$ sample. Turning to Figure 3f, the binding energy peaks of Cobalt and Oxygen manifest with atomic percentages of 45.93 and 54.09, respectively, resulting in a metal-to-oxygen ratio of 0.85 for the $Co_3O_4$ sample. These EDS findings substantiate the chemical purity of both the $Mn_3O_4$ and $Co_3O_4$ samples.

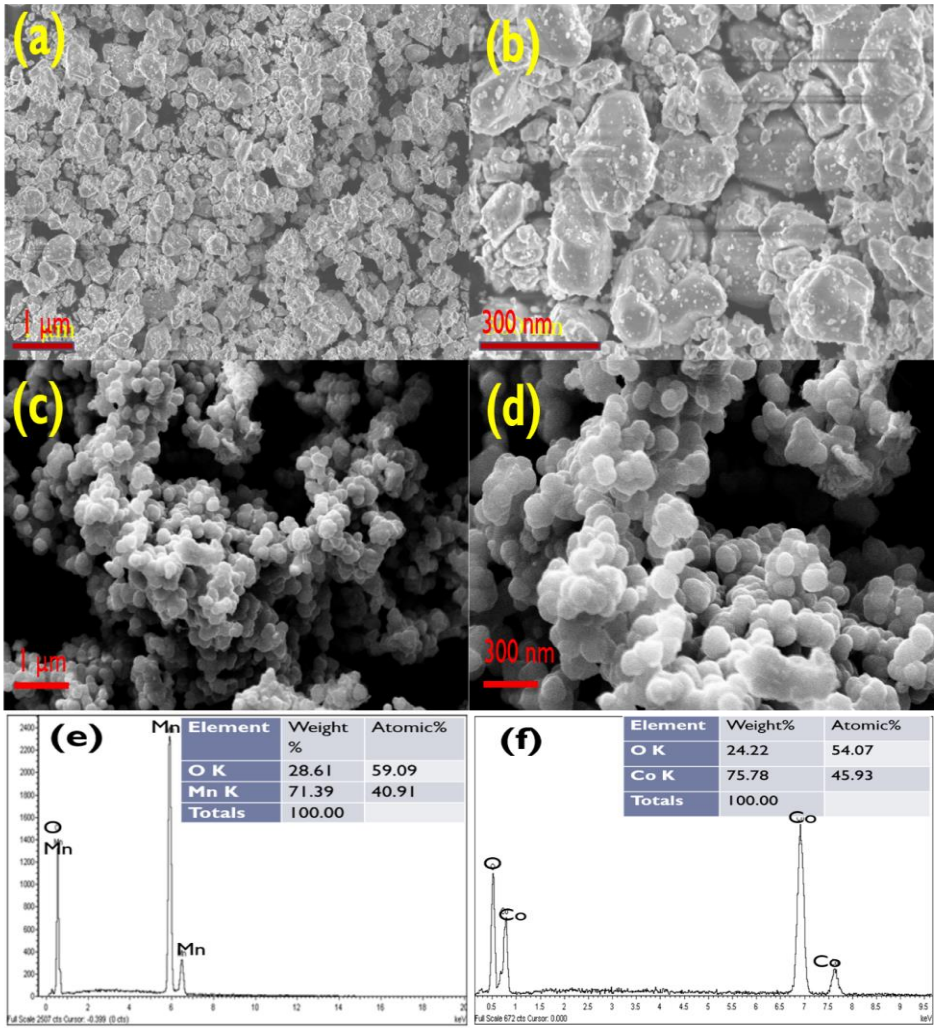


**Figure 3: (a & b) SEM images of spinel $Mn_3O_4$ and (c & d) $Co_3O_4$ nanocrystals**
**EDS of spinel (e) $Mn_3O_4$ (f) $Co_3O_4$ nanocrystals**

X-ray Photoelectron Spectroscopy (XPS) investigations were performed to assess the composition and chemical states of the samples. In the case of the $Mn_3O_4$ sample, the survey spectrum demonstrates discernible peaks attributed to Mn 3p, Mn 3s, O 1s, and Mn 2p, as illustrated in Figure 4a. The Mn 2p spectrum in Figure 4b displays binding energy peaks at 641.25 eV (Mn 2p3/2) and 653.16 eV (Mn 2p1/2), featuring a separation of 11.91 eV. Figure 4c portrays the Mn 3s spectrum, revealing two low binding energy peaks at 82.62 eV and 88.64 eV, with a gap of 5.71 eV between them. Additionally, the XPS spectrum of O 1s [Figure 4d] manifests around 532 eV, confirming the presence of oxygen within the sample. The observed energy disparities between Mn 3s and Mn 2p peaks harmonize with earlier findings [25].

For the $Co_3O_4$ sample, Figure 4e captures the Co 2p spectrum, demonstrating peak division at 780 eV (Co 2p3/2) and 795 eV (Co 2p1/2) with a separation of 15 eV [28]. This spectrum solidifies the identification of cobalt and its particular chemical state within the $Co_3O_4$ nanocrystals.

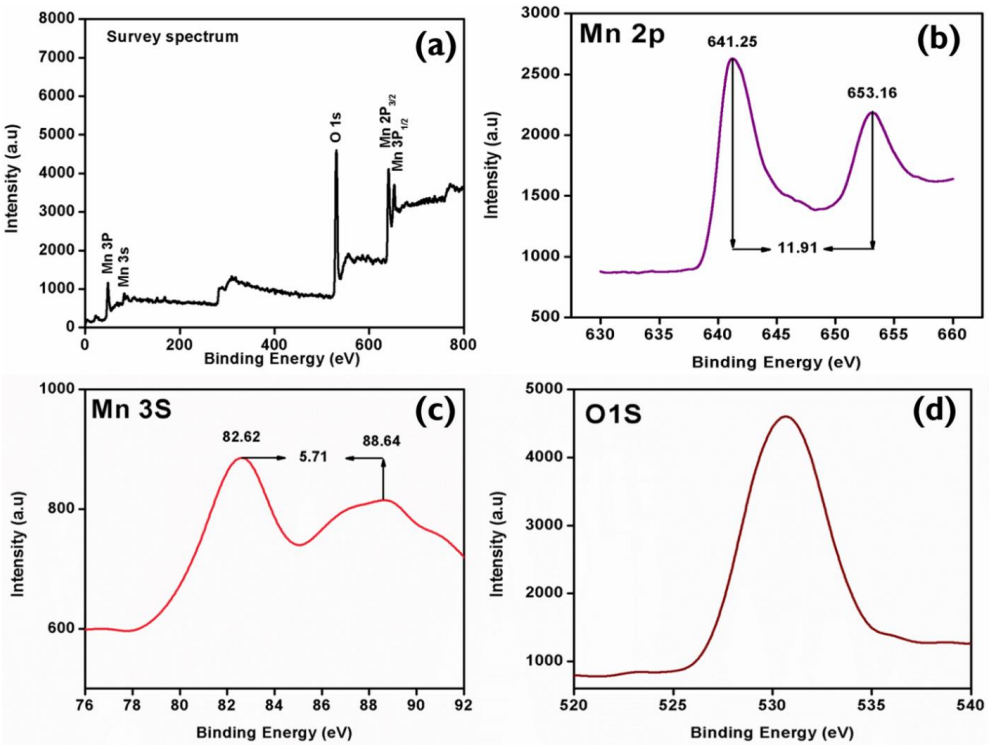


**Figure 4: $Mn_3O_4$ nanocrystals -X-ray Photoelectron spectra (a) Survey spectrum, (b) Mn 2p (c) Mn 3s and (d) O 1s.**

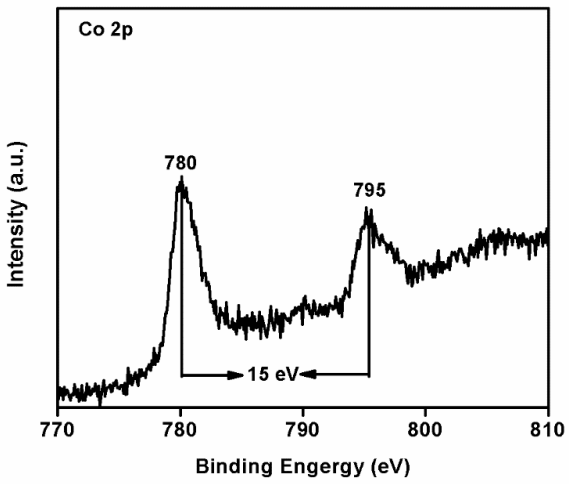


**Figure 4(e) XPS spectra of $Co_3O_4$ nanocrystals**

### B. Optical and Magnetic properties

UV-Visible spectroscopy was employed to investigate the optical characteristics of the synthesized nanocrystals within the wavelength of about 300-1000 nm to evaluate their optical band gap. The derived spectra for optical band gap, alongside the absorption spectra (visible in the inset of Figure 5), were observed. Demonstrating a semiconductor nature of p-type, the nanocrystals exhibited substantial absorption within the visible range. By utilizing an appropriate equation [29], the optical band gap values for the $Mn_3O_4$ and $Co_3O_4$ nanocrystals were calculated to be 2.93 eV and 2.5 eV, respectively.

It's noteworthy that the determined Eg values for $Mn_3O_4$ and $Co_3O_4$ nanocrystals in our study are higher than those reported in previous research [30]. This rise in the band gap is attributed to the quantum confinement effects and the presence of oxygen vacancies within the $Mn_3O_4$ and $Co_3O_4$ nanoparticles [31-34]. These factors influence electronic structure and energy levels, leading to an elevated optical band gap in the synthesized nanocrystals

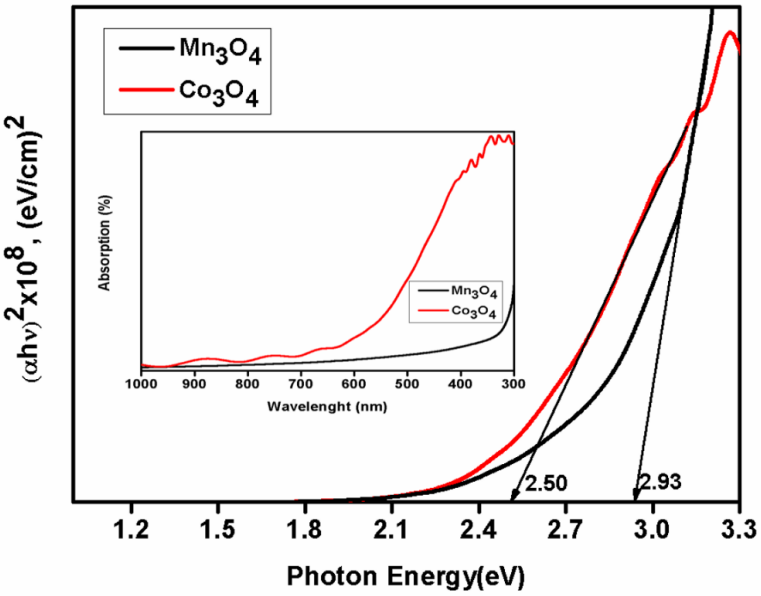


**Figure 5: Optical band gaps of $Co_3O_4$ and $Mn_3O_4$ nanocrystals**

The Vibrating Sample Magnetometer (VSM) was employed to examine the magnetic characteristics of $Mn_3O_4$ and Co3O4 nanocrystals across a temperature span of 5 K to 300 K, as depicted in Figure 6. The magnetic attributes of intricate oxides such as $Mn_3O_4$ and $Co_3O_4$, possessing regular spinel structures, are acknowledged to exhibit significant sensitivity to variations in oxygen contentIn our study, the stoichiometry of oxygen of the synthesised $Mn_3O_4$ and $Co_3O_4$ nanocrystals was determined to be $Mn_3O_{4.06}$ and $Co_3O_{3.9}$, respectively, indicating oxygen excess and deficit in the respective samples. The stoichiometric Mn3O4.06 sample exhibited ferromagnetic properties, as shown in Fig. 6a&b, with the magnetization curve at 5 K displaying a hysteresis loop characteristic of ferromagnetism. At 300 K, the curve resembled paramagnetic behavior.

The prevailing oxidation state of manganese cations within the octahedral coordination of oxygen cations was determined, predominantly constituting $Mn^{3+}$ (70.9%), accompanied by a lesser proportion of $Mn^{4+}$ (19.1%). In the context of the $Mn_3O_4$.06 sample, it was established that the remanence magnetization (Mr) stood at 0.199 emu $g^{-1}$, while the coercivity (Hc) value was measured at 1.06 kOe.

Conversely, distinct characteristics emerged in the Co3O3.9 sample. Figure 6c & d illustrates its weak ferromagnetic traits, indicated by a saturation magnetization of 0.25 emu $g^{-1}$ under a magnetic field of 0.7 kOe. The transformation from the bulk $Co_3O_4$'s antiferromagnetic state to the $Co_3O_{3.9}$ nanocrystals' weak ferromagnetic state can be ascribed to surface spins that remain uncompensated or finite size effects. It is well-recognized that the magnetic attributes of nanomaterials hinge greatly on factors such as particle dimensions, shape, crystallinity, and magnetization orientation. Thus, the $Co_3O_{3.9}$ sample can be seen as a ferromagnetic

matrix housing antiferromagnetic clusters, a consequence of the presence of oxygen vacancies that give rise to antiferromagnetic interactions.

In conclusion, the magnetic behavior of nanocrystalline $Co_3O_4$ and $Mn_3O_4$ is influenced by oxygen stoichiometry and the presence of oxygen vacancies, leading to weak ferromagnetic and ferromagnetic properties, respectively. The interplay between antiferromagnetic and ferromagnetic interactions leads to the emergence of the spin glass state within the $Co_3O_{3.9}$ nanocrystals.

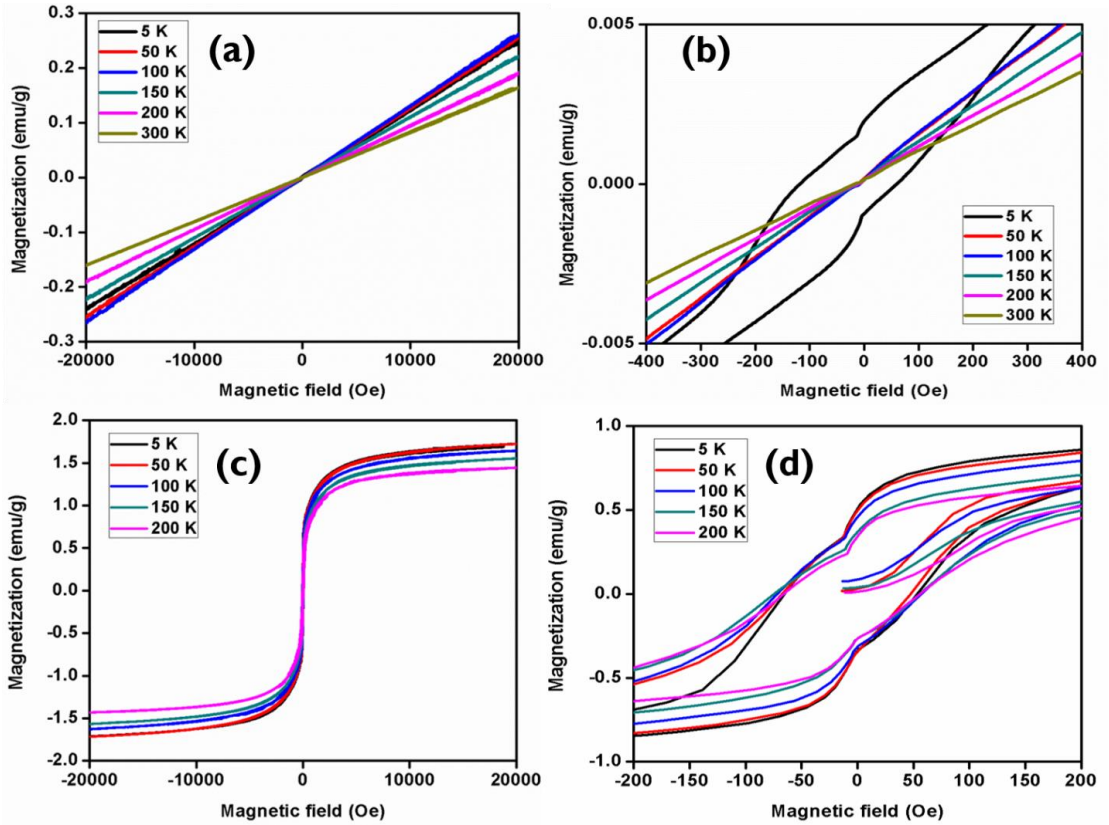


**Figure 6- a & b) M–H curves of $Mn_3O_4$ and (c & d) $Co_3O_4$ nanocrystals at 5K to 300 K.**

**C. Dielectric properties**

The capacitive response of the $Mn_3O_{4.06}$ specimen is examined through an assessment of how capacitance changes with both frequency and potential, as portrayed in Figure 7a and 7b. The graph in Figure 7a illustrates a noticeable pattern: capacitance is more pronounced at lower frequencies but diminishes as frequency escalates. Ultimately, the value stabilizes at higher frequencies. This phenomenon is attributed to the presence of space charge polarization, which loses significance at greater frequencies, thus culminating in a frequency-independent demeanor. Furthermore, the specimen's capacitance registers an upswing with escalating temperatures, as scrutinized across temperatures spanning 313 K to 373 K.

In addition, an exploration into the $Mn_3O_{4.06}$ sample's capacitance variance concerning potential at diverse temperatures is depicted in Figure 7b. Evidently, a reduction in oxygen vacancies corresponds to heightened sample conductivity, thereby bestowing enhanced electrochemical characteristics [36].

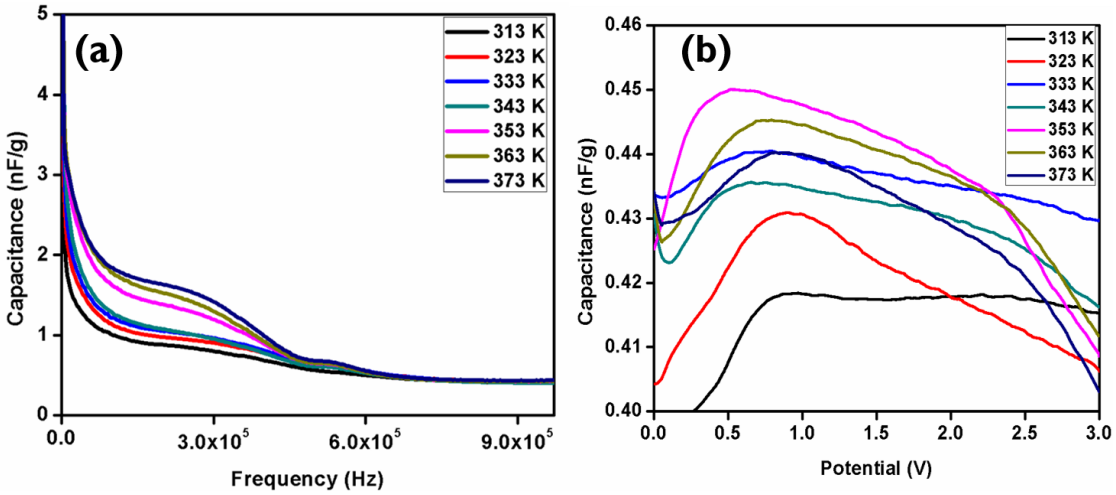


**Figure 7: (a) Dependence of AC Capacitance on frequency (b) Capacitance on potential of $Mn_3O_4$ nanocrystals**

**D. Electrochemical properties**

Nanocrystals of $Mn_3O_4$ and $Co_3O_4$, are subjected to Cyclic Voltammetry study in a one Molar $Na_2SO_4$ aqueous solution. The CV experiments are conducted at different scan rates: 1-50 mV/s for $Mn_3O_4$ and 1-10 mV/s for $Co_3O_4$. The potential window range for the experiments is -0.1 V to +0.9 V for $Mn_3O_4$ and -0.1 V to 0.7 V for $Co_3O_4$. The cyclic voltammograms obtained from the experiments are described. The CV curves for both $Mn_3O_4$ and $Co_3O_4$ show rectangular and semi-rectangular shapes. These shapes suggest that there are no distinct redox peaks in the curves. The absence of redox peaks in the CV curves indicates that the observed behavior might be due to interface capacitance between the electrode and the electrolyte. Interface capacitance is related to the ability of the electrode to store charge at the interface with the electrolyte. When the scan rate increases, the area under the CV curves also increases. This indicates that more charge is being transferred during the experiment. However, the specific capacitance decreases with higher scan rates. This could be because at higher scan rates, the movement of electrolytic ions is limited, resulting in reduced charge storage capacity. Despite the changes in the CV curve characteristics with varying scan rates, the overall shape of the CV curves remains consistent. This consistency suggests that the samples ($Mn_3O_4$ and $Co_3O_4$) are chemically stable under the experimental conditions. Equation (2) below refers to a formula used to calculate the specific capacitance (C) of the samples from the cyclic voltammetry (CV) data and the results are shown in Table 1 [25, 38, 39].

$$C = \frac{\int I(V)\,dV}{(2m\,\Delta V\,(V_2 - V_1))} \qquad \text{---} \qquad (2)$$

where, $\int I(V)\,dV =$ total voltammetric charge in coulombs, , $m =$ mass of the active electrode in grams, , $\Delta V =$ scan rate in V/s and $(V_2 - V_1) =$ potential window range in V. In Table 1, the specific capacitance values decrease with an increase in the scan rate. This observation is attributed to the fact that at lower scan rates, there is sufficient time for the electrolyte ions to occupy almost all the active sites of the electrode material, resulting

in higher specific capacitance. On the contrary, at higher scan rates, the limited time available for the electrolyte ions to reach the electrode surface leads to a lower specific capacitance.

Chronopotentiometry studies revealed the capacitive nature of the samples. Figures 8(c) & (d) demonstrate the charge-discharge cycles of the samples at various current densities. Nanocrystalline $Mn_3O_4$ exhibits symmetric charge-discharge curves, indicating high electrochemical reversibility and exceptional capacitive behavior, which corroborates the cyclic voltammetry results. Conversely, the charge-discharge curves of the $Co_3O_4$ nanocrystals are not symmetric, with lower discharge time. The discharge capacitance (C) was obtained with the help of the formula given below

$$C = \frac{I\,\Delta t}{\Delta V\, m} \qquad \text{----} \qquad (3)$$

where, I= current in amperes, $\Delta t =$ discharging time in seconds, , V= potential window in volts and m= mass of active electrode material in grams. [25]

$Mn_3O_4$ and $Co_3O_4$ nanocrystals demonstrated distinct discharge capacitance values at 0.5 A/g current density, reaching 417 and 214 Fg-1, respectively. These specific capacitance values were calculated and listed in Table 2 for various current densities. The results from the constant potential (CP) studies aligned with the cyclic voltammetry (CV) findings.

A critical factor in supercapacitors is their long-standing cyclic stability. To assess this, $Mn_3O_4$ charge-discharge cycles were conducted for ten thousand cycles at a current density of 2 A/g (Figure8(e)). Remarkably, despite 10000 cycles, 81% of capacitive retention was noticed. In contrast, $Co_3O_4$ exhibited 70% capacitive retention at 0.5 A/g current density (Figure 8(g)). The charge-discharge curves of $Mn_3O_4$ displayed a symmetric pattern with cycle number, indicating a high level of electrochemical reversibility and excellent capacitive behavior [40-44]. The columbic efficiency was determined with the formula given below (4).

$$\eta = \frac{t_d}{t_c} \times 100 \qquad \text{---} \qquad (4)$$

where, η, $t_d$ and $t_c$ are columbic efficiency, discharging time & charge time correspondingly. The $Mn_3O_4$ electrode showed 100% columbic efficacy beyond six hundred cycles as per Figure 8(e).

Electrochemical Impedance Spectroscopy (EIS) is an alternative characterization method employed for investigating the capacitive behavior of the electrode materials. EIS analysis of the sample is conducted in the frequency range from 1 Hz to 1 MHz to corroborate the CV results. The Nyquist plots of the Mn3O4 nanoparticles are shown in Figure 8(f). The juncture of the Nyquist plots on the real axis at greater frequencies signifies the solution resistance (RS). It's witnessed that both the RS and charge transfer resistances of the materials are tinier before cycling and become elevated after 10,000 cycles, that results a decline in the specific capacitance with cycles, like depicted in Figure 8(f) & (h).

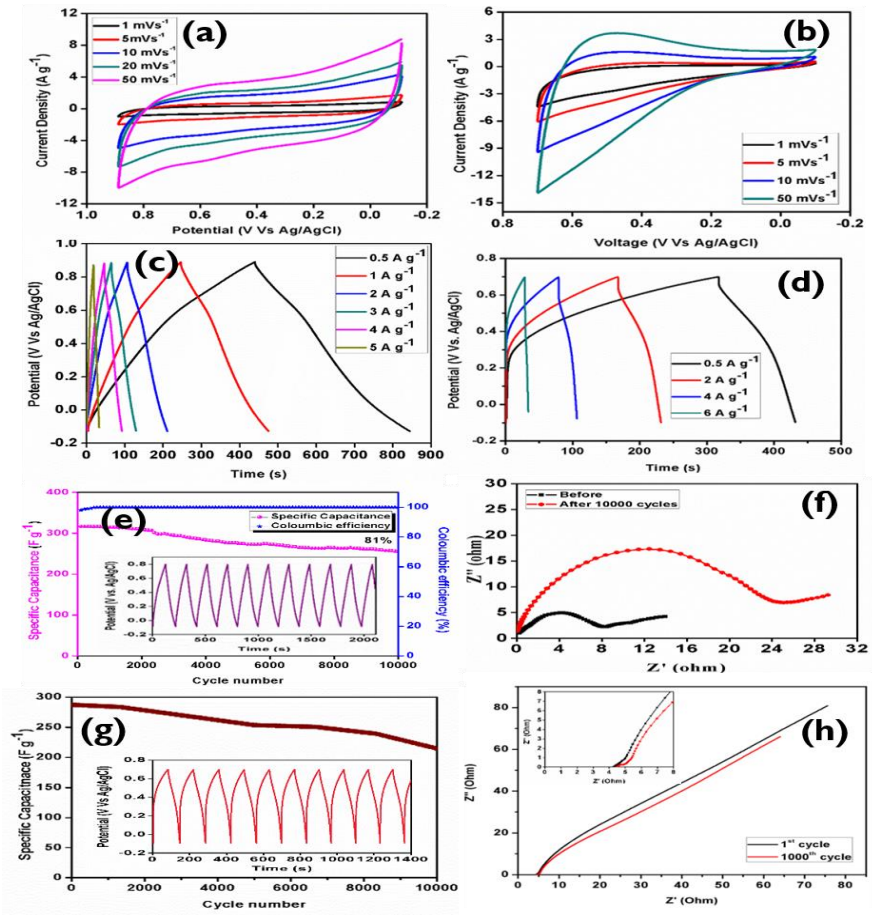


**Fig. 8: (a) Spinel $Mn_3O_4$ - cyclic voltammetry curves (b) nanocrystalline $Co_3O_4$ at various scan rates. (c) Charge-discharge curves of spinel $Mn_3O_4$ (d) Charge-discharge curves of $Co_3O_4$ nanocrystals (e) Specific capacitance and coulombic efficacy with cycle number (f) nanocrystalline $Mn_3O_4$ - Nyquist plots (g) Specific capacitance with cycle number (h) nanocrystalline $Co_3O_4$ - Nyquist plots**

## IV. CONCLUSION

$Co_3O_4$ and $Mn_3O_4$, spinel nanostructures were successfully synthesized using the solution combustion technique. XRD and Raman studies confirmed the formation of cubic shaped $Co_3O_4$, tetragonal $Mn_3O_4$ with assessed crystalline sizes of 22 nm and 14 nm, respectively. FTIR results further supported the production of cobalt oxide and manganese oxide, evident from the presence of Co-O and Mn-O bonding. The SEM micrographs showed evenly spread sphere-shaped grains with a typical size of 120 nm for $Co_3O_4$ and disseminated uneven grains of approximately 100 nm size for $Mn_3O_4$. Optical band gaps of the samples were measured to be 2.93 eV for $Mn_3O_4$ and 2.50 eV for $Co_3O_4$ nanocrystals. Additionally, they exhibited high ferromagnetism at around 5 Kelvin temperature. The electrochemical characterization studies, including CV, Chronopotentiometry, and EIS, were performed in one Molar sodium sulfate aqueous electrolyte. The as-prepared $Mn_3O_4$ nanocrystals demonstrated the maximum specific capacitance of 417 F/g at a current density of 0.5 A/g, along with reliable cyclic stability and just about 100% coulombic efficacy. From the above results, we can say that nano crystalline $Mn_3O_4$ shows promise to be an exceptional material to make electrodes for applications of supercapacitor.

# REFERENCES


[1]. P Suktha, N Phattharasupakun, P Dittanet and M Sawangphruk "Charge storage mechanisms of electrospun $Mn_3O_4$ nanofibres for high-performance supercapacitors" RSC Adv., 7 (2017) 9958-9963.

[2]. J. Chmiola , G. Yushin , Y. Gogotsi , C. Portet , P. Simon and P. L. Taberna "Anomalous Increase in Carbon Capacitance at Pore Sizes Less Than 1 Nanometer" Science, 313 (2006) 1760 —1763.

[3]. P. Huang , C. Lethien , S. Pinaud , K. Brousse , R. Laloo , V. Turq , M. Respaud , A. Demortière , B. Daffos , P. L. Taberna , B. Chaudret , Y. Gogotsi and P. Simon "On-chip and freestanding elastic carbon films for micro-supercapacitors" Science, 351 (2016) 691 — 695.

[4]. D. Pech , M. Brunet , H. Durou , P. Huang , V. Mochalin , Y. Gogotsi , P.-L. Taberna and P. Simon "Ultrahigh-power micrometre-sized supercapacitors based on onion-like carbon" Nat. Nanotechnol., 5 (2010) 651 — 654.

[5]. P Naresh Kumar Reddy, Dadamiah PMD Shaik, Vattikondala Ganesh, D Nagamalleswari, K Thyagarajan, P Vishnu Prasanth "Structural, optical and electrochemical properties of TiO2 nanoparticles synthesized using medicinal plant leaf extract" Ceramics International. 45 (2019) 16251-16260

[6]. B. G. S. Raj , R. N. R. Ramprasad , A. M. Asiri , J. J. Wu and S. Anandan "Ultrasound assisted synthesis of $Mn_3O_4$ nanoparticles anchored graphene nanosheets for supercapacitor applications" Electrochim. Acta, 156 (2015) 127 —137.

[7]. L. Yang , S. Cheng , X. Ji , Y. Jiang , J. Zhou and M. Liu "Investigations into the origin of pseudocapacitive behavior of $Mn_3O_4$ electrodes using in operando Raman spectroscopy" J. Mater. Chem. A 3 (2015) 7338 —7344.

[8]. G. S. Gund , D. P. Dubal , B. H. Patil , S. S. Shinde and C. D. Lokhande "Enhanced activity of chemically synthesized hybrid graphene oxide/$Mn_3O_4$ composite for high performance supercapacitors" Electrochim. Acta 92 (2013) 205 —215.

[9]. C.-H. Yang , I. W. Sun , C.-T. Hsieh , T.-Y. Wu , C.-Y. Su , Y.-S. Li and J.-K. Chang "Facile electrochemical preparation of hierarchical porous structures to enhance manganese oxide charge-storage properties in ionic liquid electrolytes" J. Mater. Chem. A 4 (2016) 4015 —4018.

[10]. M.-J. Deng , P.-J. Ho , C.-Z. Song , S.-A. Chen , J.-F. Lee , J.-M. Chen and K.-T. Lu "Fabrication of Mn/Mn oxide core–shell electrodes with three-dimensionally ordered macroporous structures for high-capacitance supercapacitors" Energy Environ. Sci. 6 (2013) 2178 —2185.

[11]. M.-J. Deng , J.-K. Chang , C.-C. Wang , K.-W. Chen , C.-M. Lin , M.-T. Tang , J.-M. Chen and K.-T. Lu "High-performance electrochemical pseudo-capacitor based on $MnO_2$ nanowires/Ni foam as electrode with a novel Li-ion quasi-ionic liquid as electrolyte" Energy Environ. Sci. 4 (2011) 3942 —3946.

[12]. T. Ngoc, T. Pham and Y S Yoon "Development of Nanosized $Mn_3O_4$-$Co_3O_4$ on Multiwalled Carbon Nanotubes for Cathode catalyst in urea fuel cell" Energies 13 (2020) 2322-2335

[13]. R. Regmi, R. Tackett, G. Lawes Journal of Magnetism and Magnetic Mateirals "Suppression of low-temperature magnetic states in $Mn_3O_4$ nanoparticles" 321 (2009) 2296-2299.

[14]. Vipin C. Bose, V. Biju, "Optical, electrical and magnetic properties of nanostructured $Mn_3O_4$ synthesized through a facile chemical route" Physica E, 66(2015) 24–32.

[15]. M.A. Almessiere, A.V. Trukhanov, F.A. Khan, Y. Slimani, N. Tashkandi, V.A. Turchenko, T.I. Zubar, D.I. Tishkevich, S.V. Trukhanov, L.V. Panina, A. Baykal, Correlation between microstructure parameters and anti-cancer activity of the $[Mn_{0.5}Zn_{0.5}](Eu_xNdxFe_{2-2x})O_4$ nanoferrites produced by modified sol-gel and ultrasonic methods, Ceram. Int. 46 (2020) 7346-7354.

[16]. M.A. Almessiere, Y. Slimani, H. Güngüneş, V.G. Kostishyn, S.V. Trukhanov, A.V. Trukhanov, A. Baykal, Impact of Eu3+ ion substitution on structural, magnetic and microwave traits of Ni-Cu-Zn spinel ferrites, Ceram. Int. 46 (2020) 11124-11131.

[17]. D.A. Vinnik, F.V. Podgornov, N.S. Zabeivorota, E.A. Trofimov, V.E. Zhivulin, A.S. Chernukha, M.V. Gavrilyak, S.A. Gudkova, D.A. Zherebtsov, A.V. Ryabov, S.V. Trukhanov, T.I. Zubar, L.V. Panina, S.V. Podgornaya, M.V. Zdorovets, A.V. Trukhanov, Effect of treatment conditions on structure and magnetodielectric properties of barium hexaferrites, J. Magn. Magn. Mater. 498 (2020) 166190.

[18]. A.L. Kozlovskiy, I.E. Kenzhina, M.V. Zdorovets, FeCo-Fe2CoO4/Co3O4 nanocomposites: Phase transformations as a result of thermal annealing and practical application in catalysis, Ceram. Int. 46 (2020) 10262-10269.

[19]. K. Dukenbayev, I.V. Korolkov, D.I. Tishkevich, A.L. Kozlovskiy, S.V. Trukhanov, Y.G. Gorin, E.E. Shumskaya, E.Y. Kaniukov, D.A. Vinnik, M.V. Zdorovets, M. Anisovich, A.V. Trukhanov, D. Tosi, C. Molardi, Fe3O4 nanoparticles for complex targeted delivery and boron neutron capture therapy, Nanomaterials-Basel 9 (2019) 494.

[20]. D.I. Tishkevich, I.V. Korolkov, A.L. Kozlovskiy, M. Anisovich, D.A. Vinnik, A.E. Ermekova, A.I. Vorobjova, E.E. Shumskaya, T.I. Zubar, S.V. Trukhanov, M.V. Zdorovets, A.V. Trukhanov, Immobilization of boron-rich compound on Fe3O4 nanoparticles: Stability and cytotoxicity, J. Alloys Compd. 797 (2019) 573-581.

[21]. M.A. Almessiere, A.V. Trukhanov, Y. Slimani, K.Y. You, S.V. Trukhanov, E.L. Trukhanova, F. Esa, A. Sadaqat, K. Chaudhary, M. Zdorovets, A. Baykal, Correlation between composition and electrodynamics properties in nanocomposites based on hard/soft ferrimagnetics with strong exchange coupling, Nanomaterials-Basel 9 (2019) 202.

[22]. M.V. Zdorovets, A.L. Kozlovskiy, Study of phase transformations in Co/CoCo2O4 nanowires, J. Alloys Compd, 815 (2020) 152450.

[23]. Lorenzo Bigiani, Mariam Hassan, Davide Peddis, Chiara Maccato, Gaspare Varvaro, Cinzia Sada, Elza Bontempi, Sara Martí-Sanchez, Jordi Arbiol and Davide Barreca, High Magnetic Coercivity in Nanostructured $Mn_3O_4$ Thin Films Obtained by Chemical Vapor Deposition. DOI: 10.1021/acsanm.9b00141

[24]. A.D. Khalajia, M. Soleymanifarda M. Jarosovab and P. Machek, Facile Synthesis and Characterization of $Mn_3O_4$, $Co_3O_4$, and NiO, Acta Physica Polonica A, 6 137 (2020), 1043-1045

[25]. Dadamiah PMD Shaik, P. Rosaiah, Y Qiu and O. M. Hussain, "Hydrothermally synthesized porous $Mn_3O_4$ nanoparticles with enhanced electrochemical performance for supercapacitors" Ceramics International, 45(2) (2019), 2226-2233.

[26]. N. Mironova-Ulmanea, A. Kuzmina, V. Skvortsova, G. Chikvaidze, I. Sildos, J. Grabisc, D. Jankovi, A. Dindune and M. Maiorov, Synthesis and Vibration Spectroscopy of Nano-Sized Manganese Oxides, Acta Physica Polonica A, 4 133 2018 1013-1016.

[27]. Saeed Farhadi, Masoumeh Javanmard and Gholamali Nadri, Characterization of Cobalt Oxide Nanoparticles Prepared by the Thermal Decomposition of $[Co(NH_3)_5(H_2O)](NO_3)_3$ Complex and Study of Their Photocatalytic Activity

[28]. Thi Ngoc Tuyen Pham and Young Soo Yoon" Development of Nanosized $Mn_3O_4$-$Co_3O_4$ on Multiwalled Carbon Nanotubes for Cathode Catalyst in Urea Fuel Cell" Energies 2020, 13, 2322, Energies 2020, 13, 2322

[29]. SubhashThota, AshokKumar, JitendraKumar "Optical, electrical and magnetic properties of $Co_3O_4$ nanocrystallites obtained by thermal decomposition of sol–gel derived oxalates" 164 (2009) 30-37.

[30]. Saeed Farhadi, Jalil Safabakhsh and Parisa Zaringhadam, Synthesis, characterization, and investigation of optical and magnetic properties of cobalt oxide ($Co_3O_4$) nanoparticles. Journal Of Nanostructure in Chemistry1-9.

[31]. S.V. Trukhanov, I.O. Troyanchuk, N.V. Pushkarev, H. Szymczak, The influence of oxygen deficiency on the magnetic and electric properties of La0.70Ba0.30MnO3-γ ($0 \leq \gamma \leq 0.30$) manganite with a perovskite structure, JETP 95 (2002) 308-315.

[32]. I.Z. Zhumatayeva, I.E. Kenzhina, A.L. Kozlovskiy, M.V. Zdorovets, The study of the prospects for the use of Li0.15Sr0.85TiO3 ceramics, J. Mater. Sci.: Mater. Electron. 31 (2020) 6764–6772.

[33]. S.V. Trukhanov, V.A. Khomchenko, L.S. Lobanovski, M.V. Bushinsky, D.V. Karpinsky, V.V. Fedotova, I.O. Troyanchuk, A.V. Trukhanov, S.G. Stepin, R. Szymczak, C.E. Botez, A. Adair, Crystal structure and magnetic properties of Ba-ordered manganites Ln0.70Ba0.30MnO3−δ (Ln = Pr, Nd), JETP 103 (2006) 398–410.

[34]. K.K. Kadyrzhanov, D.I. Shlimas, A.L. Kozlovskiy, M.V. Zdorovets, Research of the shielding effect and radiation resistance of composite CuBi2O4 films as well as their practical applications. J. Mater. Sci.: Mater. Electron. 31 (2020) 11729–11740.

[35]. S. Fritsch, J. Sarrais, A. Rousset and G.U. Kulkarni "Low-temperature oxidation of Mn3O4 Hausmannite" Materials Research Bulletin, 33 (1998) 1185-1194.
[36]. I.O. Troyanchuk, S.V. Trukhanov, D.D. Khalyavin, H. Szymczak, Magnetic properties of anion deficit manganites Ln0.55Ba0.45MnO3-γ (Ln=La, Nd, Sm, Gd, $\gamma \leqslant 0.37$), J. Magn. Magn. Mater. 208 (2000) 217-220.

[37]. S.V. Trukhanov, A.V. Trukhanov, A.N. Vasil'ev, A. Maignan, H. Szymczak, Critical behavior of La0.825Sr0.175MnO2.912 anion-deficient manganite in the magnetic phase transition region, JETP Lett. 85 (2007) 507-512.

[38]. Vijaya Sankar K, Kalpana D, Kalai Selvan R " Electrochemical Properties of microwave-assisted reflux-synthesized $Mn_3O_4$ nanoparticles in different electrolytes for supercapacitor applications" Journal of Applied Electrochemistry 42 (2012) 463-470.
[39]. Lu-Feng Y, Chuang G, Ming-Tao Z, Chao-Fan H, Jiang-Hu C, Ying-Liang L "Synthesis and Electrochemical properties of $Mn_3O_4$ polyhedral nanocrystals" Chinese Journal of Inorganic Chemistry 29(2013) 381-388.
[40]. H. Jiang, T. Zhao, C.Y. Yan, J. Ma, C. Z. Li " Hydrothemal synthesis of novel $Mn_3O_4$ nano-octahedrons with enhanced supercapacitors performances" Nanoscale 2 (2010) 2195-2198
[41]. Ghodbane O, Pascal J L, Fraisse B, Favier F. "Structural in situ study of the Thermal behavior of Manganese dioxide material:Toward selected electrode materials for supercapacitors" ACS applied materials and Interfaces 2 (2010) 3493-3505
[42]. H. Jiang, T. Zhao, C.Y. Yan, J. Ma, C. Z. Li "High–rate electrochemical capacitors from highly graphitic carbon–tipped manganese oxide/mesoporous carbon/manganese oxide hybrid nanowires" Nanoscale 2, 2195 (2010)
[43]. CM Julien, M. Massot, C. Poinsignon "Lattice vibrations of manganese oxides. Part I. Periodic structures" Spectrochimica Acta A 60(2004) 689-700
[44]. Shuang-Yu Liu, Jian Xie, Yun-Xiao Zheng, Gao-Shao Cao, Tie-Jun Zhu, Xin-Bing Zhao "Nanocrystal manganese oxide ($Mn_3O_4$, MnO) anchored on graphite nanosheet with improved electrochemical Li-storage properties" Electrochimica Acta 66 (2012) 271-278.